

# Sign-reversal of the in-plane resistivity anisotropy in hole-doped iron pnictides

E. C. Blomberg,<sup>1,2</sup> M. A. Tanatar,<sup>1,2</sup> R. M. Fernandes,<sup>3</sup> I. I. Mazin,<sup>4</sup> Bing Shen,<sup>5,6</sup> Hai-Hu Wen,<sup>5,6</sup> M. D. Johannes,<sup>4</sup> J. Schmalian,<sup>7</sup> and R. Prozorov<sup>1,2</sup>

<sup>1</sup>The Ames Laboratory, Ames, Iowa 50011, USA

<sup>2</sup>Department of Physics and Astronomy, Iowa State University, Ames, Iowa 50011, USA

<sup>3</sup>School of Physics and Astronomy, University of Minnesota, Minneapolis, MN 55455, USA

<sup>4</sup>Naval Research Laboratory, Code 6390, Washington, DC 20375, USA

<sup>5</sup>Institute of Physics, Chinese Academy of Sciences, Beijing 100190, P. R. China

<sup>6</sup>National Laboratory of Solid State Microstructures and Department of Physics, Nanjing University, Nanjing 210093, P. R. China

<sup>7</sup>Institute for Theory of Condensed Matter Physics and Center for Functional Nanostructures, Karlsruhe Institute of Technology, Karlsruhe, 76131, Germany

(Dated: 20 November 2012)

**The concept of an electronically-driven breaking of the rotational symmetry of a crystal [1], without involving magnetic order, has found experimental support in several systems, from semiconductor heterostructures [2] and ruthenates [3], to cuprate [4] and iron-pnictide [5] superconductors. In the pnictide  $\text{BaFe}_2\text{As}_2$ , such an “electronic nematic state” appears above the magnetic transition dome, over a temperature range that can be controlled by external strain [6, 7]. Here, by measuring the in-plane resistivity anisotropy, we probe the electronic anisotropy of this material over the entire nematic/magnetic dome, whose end points coincide with the optimal superconducting transition temperatures. Counter-intuitively, we find that, unlike other materials, the resistivity anisotropy in  $\text{BaFe}_2\text{As}_2$  changes sign across the doping phase diagram, even though the signs of the magnetic, nematic, and orthorhombic order parameters are kept fixed. This behavior is explained by the Fermi surface reconstruction in the magnetic phase and spin-fluctuation scattering in the nematic phase. The unique behavior of the transport anisotropy unveils that the primary role is played by magnetic scattering in the normal state transport properties of the iron pnictides, suggesting a close connection between magnetism, nematicity, and unconventional superconductivity.**

Superconductivity in all iron-based superconductors is found in the proximity of magnetic order, which is preceded or accompanied by a structural transition (see [8, 9] for review). In the family of  $A\text{Fe}_2\text{As}_2$  ( $A=\text{Ca}, \text{Sr}, \text{Ba}, \text{Eu}$ ) compounds, the magnetic order below  $T_N$  is a uniaxial stripe type [10], with in-plane ordering vectors  $(\pi, 0)$  or  $(0, \pi)$ . The structural transition at  $T_s \geq T_N$  preempts the magnetic stripe ordering and reduces the tetragonal symmetry of the lattice to orthorhombic. It has been suggested by several experiments [5, 11–13] and theories [14–17] that the tetragonal symmetry breaking is caused by magnetic, i.e. electronic, rather than elastic degrees of freedom, giving rise to an electronic nematic phase, see Fig. 1. Doping of the parent  $\text{BaFe}_2\text{As}_2$  with electrons (by Co substitution of Fe,  $\text{BaCo122}$ ) or holes (by K substitution of Ba,  $\text{BaK122}$ ) suppresses both magnetic and nematic orders, revealing superconductivity with a maximum  $T_c$  close to the edges of the magnetic/nematic dome, Fig. 1.

Below  $T_s$ , the sample splits into structural twin domains with different directions of the orthorhombic  $a_o$  and  $b_o$  axes ( $a_o > b_o$ ) [18]. Applying a small uniaxial strain not only stabilizes one particular domain below  $T_s$ , but also extends the nematic phase to temperatures well above  $T_s$ , due to the coupling between the strain field and nematic fluctuations (red area in Fig. 1) [13, 19, 20]. In

these strained samples, the nematic state anisotropy reveals itself not only in the small orthorhombic distortion  $a_o - b_o \ll a_o + b_o$ , but, mostly, in a pronounced anisotropy of the in-plane electrical resistivity  $\varrho \equiv \rho_b/\rho_a - 1$  [6, 7, 21]. Regardless of the microscopic nature of the nematic order parameter,  $\varphi$ , symmetry imposes that close to the nematic transition temperature  $\varrho = \kappa \varphi$ , where  $\kappa$  is a coupling parameter. Indeed, this relation was verified experimentally in the parent compound of  $\text{BaFe}_2\text{As}_2$  [19]. Unsurprisingly, in the only system where the electronic anisotropy was systematically studied across the nematic dome, the ruthenate  $\text{Sr}_3\text{Ru}_2\text{O}_7$  [3],  $\varrho$  was found to retain the same sign across the phase diagram.

In the  $\text{BaFe}_2\text{As}_2$  family, most of the studies on its nematicity have focused on the electron-doped compounds, finding  $\varrho > 0$  in both magnetic and nematic phases [6, 7, 22]. More recently, experiments in underdoped  $\text{BaK122}$  found a rather small, but still positive, value of  $\varrho$  [21]. Here we report that for larger K-doping levels, not explored in the previous studies, the anisotropy  $\varrho$  changes sign both near  $T_s$  (nematic phase) and at very low temperatures (magnetically ordered phase). Since the sign of  $\varphi$  is fixed by the small applied uniaxial strain, the coupling parameter  $\kappa$  must change sign across the magnetic/nematic dome. We interpret this sign-change as a result of asymmetric changes in the magnetic scatter-

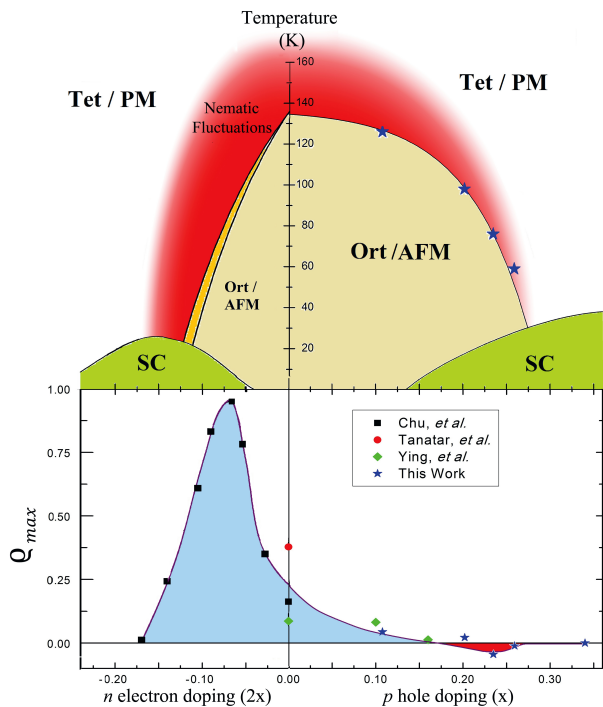


FIG. 1. (Color Online) Top panel: Phase diagram of the electron- and hole-doped Ba122 system focusing on the under-doped regime with superconducting region shown in green. The domain of the orthorhombic (antiferromagnetic) phase below transition from the tetragonal phase,  $T_S$ , is shown in yellow. Nematic fluctuations (red region) persist far above  $T_S$  and affect the in-plane resistivity anisotropy in strained samples. The lower panel shows the maximum in-plane anisotropy  $\varrho_{\max}$  as a function of doping. Note the significant asymmetry of  $\varrho_{\max}(x)$  and its sign change in the hole-doped regime.

ing and in the magnetically reconstructed band structure for electron and hole doping. This unique complexity of the nematic dome observed in the iron pnictides suggests that spin-scattering dominates transport in the normal state, establishing a possible connection to a magnetically mediated mechanism of superconductivity.

Figure 2 presents our main experimental finding, the sign reversal of the in-plane resistivity anisotropy. For BaK122 samples with  $x \leq 0.202$ , the resistivity is larger along the shorter orthorhombic axis,  $\rho_a < \rho_b$ , whereas for samples with  $x \geq 0.235$ , the longer axis has higher resistivity,  $\rho_a > \rho_b$ . This is clearly seen in the inset zooming in on the structural transition region. It is also apparent that, due to the applied uniaxial strain, the in-plane anisotropy starts to appear well above the structural transition  $T_s$  of the unstrained sample.

In the bottom panel of Fig. 2 we plot the temperature-dependent anisotropy ratio,  $\varrho$ , for several compositions. We use two characteristic features of the  $\varrho(T)$  curves to further analyze the data. First, we plot in the bottom panel of Fig. 1 the maximum in-plane anisotropy  $\varrho_{\max}$  for different  $x$ . In the upper panel of Fig. 3, we plot

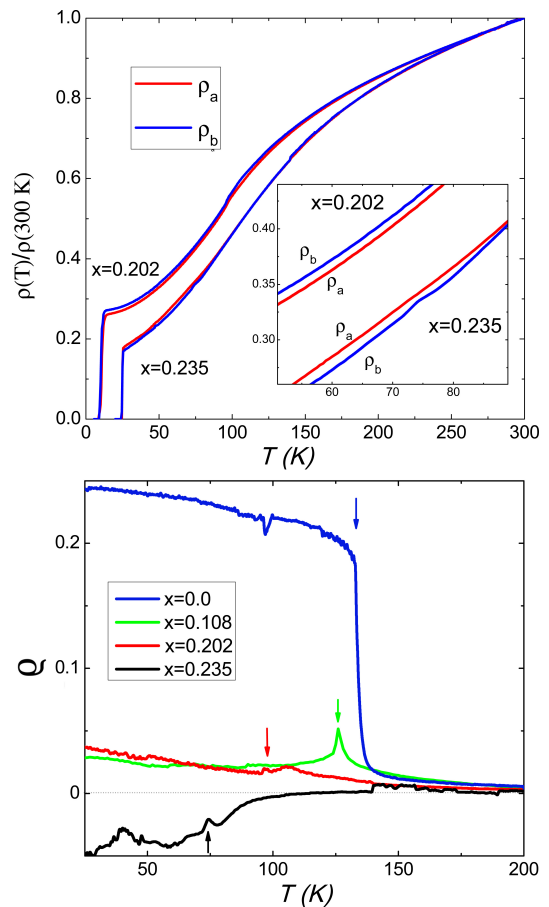


FIG. 2. (Color Online) Upper panel: Normalized temperature-dependent resistivity,  $\rho(T)/\rho(300K)$ , for the BaK122 samples with  $x = 0.202$  and  $x = 0.235$ . The red lines show the resistivity along the  $a_o$ -axis ( $\rho_a$ ) while the blue lines show  $\rho_b$ . The inset zooms at the structural transition, where a clear reversal of the anisotropy from  $\rho_b > \rho_a$  for  $x = 0.202$  to  $\rho_b < \rho_a$  for  $x = 0.235$  occurs. Lower panel: temperature dependence of  $\varrho$  for different K-doping levels. The arrows mark the magnetic transition temperatures.

$\varrho(T \approx T_N)$ , i.e. at temperatures immediately below the magnetic transition, which coincides with the structural transition temperature of the unstrained BaK122 samples.

An interesting general picture emerges from the analysis of the experimental observations of this and previous studies [6, 7, 21]. On the one hand, for all electron-doped BaCo122 and parent compositions, the resistivity anisotropy is positive,  $\varrho(x) > 0$ . The maximum anisotropy,  $\varrho_{\max}(x)$ , shown in the bottom panel of Fig. 1, is peaked at some intermediate electron doping, vanishing near the edge of the magnetic/nematic dome, due to the vanishing orthorhombic distortion. On the other hand, on the hole-doped side,  $\varrho_{\max}(x)$  remains positive up to moderate hole-doping, but decreases by more than one order of magnitude, from  $\varrho_{\max}(x = 0) \approx +0.3$  to  $\varrho_{\max}(x = 0.202) \approx +0.02$ . Even more surprisingly,

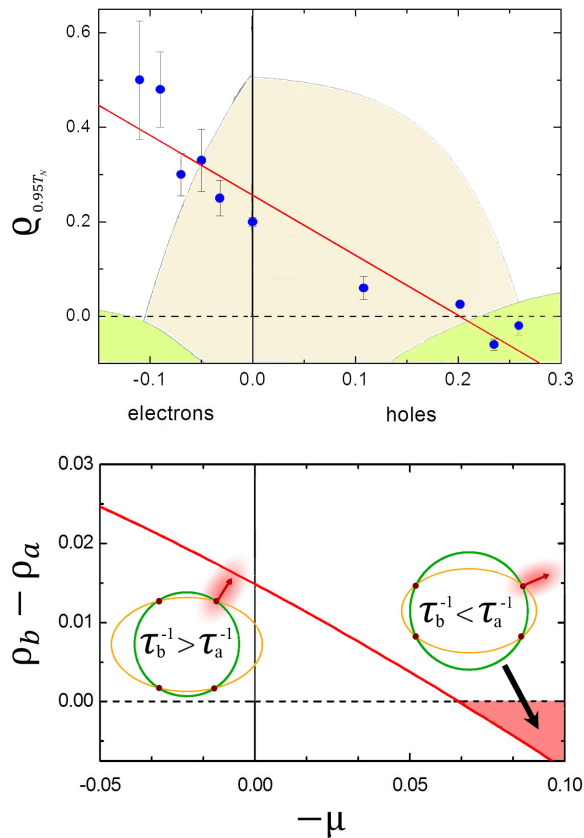


FIG. 3. Top panel: doping dependence of the in-plane resistivity anisotropy at  $0.95T_N$  in both electron- and hole-doped  $\text{BaFe}_2\text{As}_2$ . The red line is a guide to the eye. The nematic/magnetic and superconducting domes are shown in the background for reference only, without temperature scale. Bottom panel: theoretical calculation of the maximum in-plane resistivity anisotropy in the paramagnetic phase normalized by the residual resistivity,  $\rho_0$ , as a function of the chemical potential (in units of the Fermi energy). The insets show schematically the differences in the scattering rates corresponding to different Fermi velocities at the hot spots for electron- and hole-doped systems. When the hot-spot Fermi velocity has a larger component along the  $b$  ( $a$ ) direction, the magnetic scattering rate is larger along the  $b$  ( $a$ ) direction. The hot spots are obtained by displacing the electron pocket (yellow ellipse) by  $(\pi, 0)$ , making it overlap with the hole pocket (green circle). The shaded red area denotes the predicted sign reversal of the anisotropy.

$\rho_{\max}(x)$  changes sign and exhibits a minimum at a higher hole doping concentration,  $\rho_{\max}(x = 0.235) \approx -0.034$ , before it eventually approaches zero close to the edge of the magnetic/nematic dome, near  $x = 0.3$ .

This sign-change happens at all temperatures, even near  $T_N$ , as shown in the bottom panel of Fig. 2 and in the upper panel of Fig. 3. Furthermore, as it can be seen in the bottom panel of Fig. 2, the magnitude of the temperature-dependent anisotropy ratio,  $\rho(T)$ , is maximal close to  $T_N$  in the parent and slightly hole-

doped compositions, but increases monotonically on cooling for higher hole doping levels. This signals that the low-temperature anisotropic reconstruction of the band structure due to long-range magnetic order plays a progressively more important role near the hole-doped edge of the nematic/magnetic dome.

Naively, the fact that  $\rho_b > \rho_a$  across most of the phase diagram seems surprising, because the ferromagnetic direction appears to be less conducting than the antiferromagnetic one. From the orbital ordering point of view [23–25] one expects the opposite effect. However, a closer look at the Fermi surface reconstruction [7, 22] and the magnetic scattering mechanisms [26, 27] suggests that the anisotropy sign is decided by quantitative factors that depend on the electronic structure, going beyond general order parameter arguments. Moreover, the different contributions to the transport anisotropy do not necessarily compete with each other. To sort them out, we focus first on the nematic paramagnetic phase, in which scattering by magnetic fluctuations dominates and the band structure is not yet reconstructed by the magnetic order.

The experimental doping evolution of  $\rho(T \approx T_N)$ , shown in the upper panel of Fig. 3, displays a rather monotonic behavior, changing sign for sufficient hole-doping levels and vanishing at the edges of the nematic dome. Such a sign-change was previously predicted by the theoretical model of Ref. [26] for the anisotropic magnetic scattering in the nematic phase. The minimal model of Ref. [26], shown in the Supplementary Material to be consistent with first-principles calculations, consists of a circular hole pocket at the center of the square-lattice Brillouin zone and two elliptical electron pockets centered at momenta  $(\pi, 0)$  and  $(0, \pi)$ , which coincide with the magnetic-stripe ordering vectors. In the nematic phase, the amplitude of the fluctuations around these two ordering vectors becomes unequal [17], breaking the tetragonal symmetry of the system and inducing anisotropic scattering. In the experiment, the applied strain selects the  $(\pi, 0)$  fluctuations.

The work in Ref. [26] showed that, in the presence of impurities and in the low-temperature limit - but still in the paramagnetic phase - the scattering rates along  $a$  and  $b$ , and consequently the sign of the resistivity anisotropy is controlled by the Fermi velocities of the hot spots connecting the hole and electron pockets, see Fig. 3. Roughly, in electron-doped compounds, the hot-spots Fermi velocity has a larger component along the  $b$  direction, giving rise to a larger scattering rate for electrons travelling along this direction, implying  $\rho_b > \rho_a$ . As the system is doped with holes, the hole pocket expands while the electron pocket shrinks, changing the position and the Fermi velocity of the hot spots, which eventually acquires a larger component along the  $a$  direction, implying  $\rho_a > \rho_b$ . To go beyond the low-temperature paramagnetic limit and make closer connection to the experiment, we used the same model of Ref. [26] and obtained

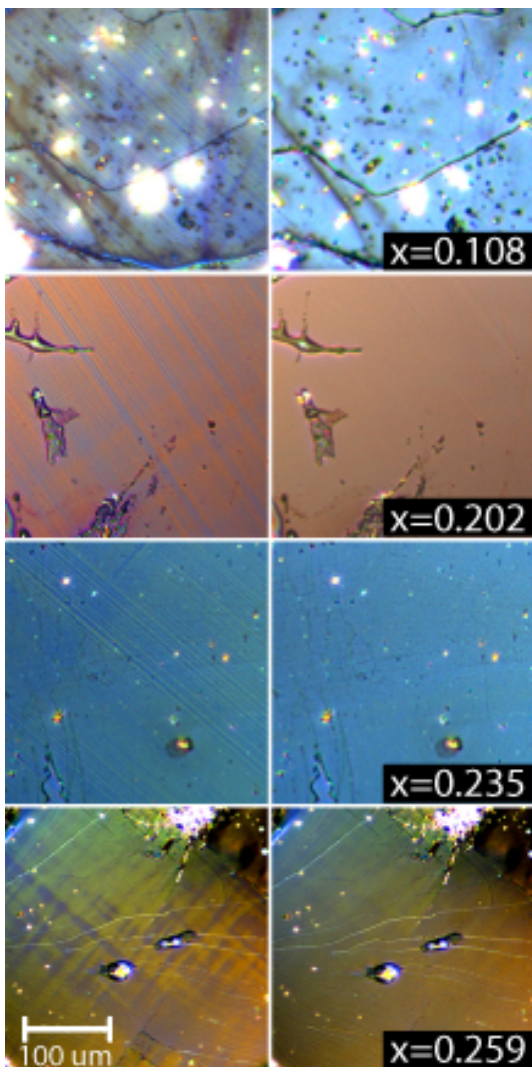


FIG. 4. (Color Online) Polarized light microscopy of BaK122 samples with doping levels as shown in the panels. Images were taken at temperatures just above the tetragonal-to-orthorhombic structural transition ( $T > T_s$ , right) and 5K ( $T < T_s$ , left), the latter showing formation of structural domains due to four different orientations of  $a_O$  and  $b_O$  axes. The difference in color of the domains is due to spectral dependence of birefractance, depending on angle between the  $a_O$  direction and the polarization plane of incident white light. Since birefractance is proportional to the orthorhombic distortion, the contrast naturally vanishes in the tetragonal phase (right panels).

numerically the maximum resistivity anisotropy in the paramagnetic phase as function of doping. The results, shown in the bottom panel of Fig. 3, agree qualitatively with the experimental data, capturing both the electron-hole asymmetry of  $\varrho(T \approx T_N)$  and its sign-change in the hole-doped regime. This suggests that magnetic scattering plays a central role in the paramagnetic phase.

Our data in Fig.2 also show that the sign-change in the resistivity anisotropy persists down to  $T = 0$ , deep

inside the magnetic state, where magnetic fluctuations are weaker. In this regime, transport should be governed by anisotropic reconstruction of the band structure. By employing first-principles calculations, we obtained the Fermi surface in the magnetically ordered state and evaluated  $\varrho$  in the relaxation-time approximation (see Supplementary Material).

Our calculations show that, in the parent compound, the reconstructed Fermi surface contains not only quasi-isotropic hole and electron pockets, but also Dirac cones whose crossing points are located slightly below the Fermi level. These features are in good agreement with quantum oscillation measurements [22]. Due to the large value of their Fermi velocities, these Dirac cones dominate the transport in the magnetic state, giving rise to an anisotropy in the resistivity that is in agreement with the experimental observations for  $x = 0$ . When holes are added to the system, the chemical potential shifts down, eventually crossing the Dirac points. Using the values extracted by ARPES [28] and quantum oscillation measurements [22], we estimate this Dirac-point crossing to happen between 0.03 and 0.1 holes/Fe. For this doping concentration, the contribution to  $\varrho$  coming from the Dirac pockets is vanishingly small, making the contribution from the remaining pockets dominant. The latter depends on details that are beyond the accuracy of first-principles calculations, and can either yield a small positive or negative  $\varrho$ . Yet, our first-principles approach correctly captures the tendency of a vanishing  $\varrho$  inside the magnetically ordered phase in the hole-doped samples.

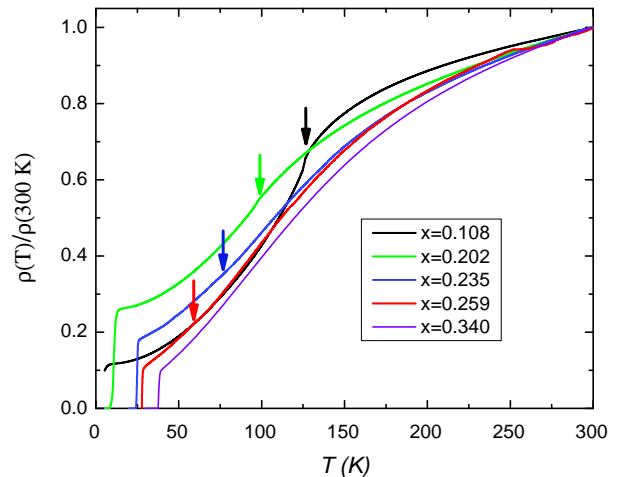


FIG. 5. (Color Online) Temperature-dependent resistivity along the orthorhombic  $a_o$ -axis,  $\rho_{a_o}$  for samples of BaK122 with four different potassium doping levels in the strain-free, twinned, state. The curves are shown using normalized plots,  $\rho(T)/\rho(300K)$ . Arrows indicate the transition temperatures and were determined by the maximum in the derivative of the resistivity and from polarized optical microscopy.

In conclusion, we observe the reversal of the in-plane

resistivity anisotropy between electron- and hole-doped BaFe<sub>2</sub>As<sub>2</sub> compounds. We attribute such behavior to the spin-fluctuation scattering in the nematic phase and to the Dirac-cones contribution in the magnetically ordered phase. Both mechanisms complementarily predict a resistivity anisotropy that is larger in the electron-doped side and continuously smaller in the hole-doped side. Our analysis shows that the change in the sign of the resistivity anisotropy can be completely understood in terms of the band structure of the pnictides, without invoking a change from itinerant to local moment physics, as suggested recently by Ref. [29]. Besides shedding light on the singular character of the nematic phase in the iron pnictides, our observation serves as a unique fingerprint for the predominance of electronic scattering due to spin fluctuations, rather than phonons, in the normal state of these superconductors. Therefore, our study provides strong support to the concept that anomalous magnetic scattering in the proximity of a putative quantum critical point is intimately connected to magnetically-mediated unconventional superconductivity [30, 31].

## SUPPLEMENTARY MATERIAL

### Methods

Single crystals of BaK122 with a size up to 7x7x1 mm<sup>3</sup> were grown from FeAs flux as described in Ref.[32]. Potassium content in the samples was determined using electron probe microanalysis with wavelength dispersive spectroscopy (WDS), see [33] for details. Samples, had typical dimensions of 0.5 mm wide, 2 to 3 mm long and 0.05 mm thick, and were cut from cleaved slabs along the tetragonal [110] direction (which becomes either the orthorhombic  $a_o$  or  $b_o$  axis below  $T_{SM}$ ). Optical imaging was performed on the samples while mounted on a cold finger in a continuous flow liquid helium cryostat (allowing for precise temperature control in 5K to 300K range) using a *Leica DMLM* microscope.

Polarized light microscopy was used for visualization of the structural domains [18] and the sample selection was based on the clarity of domains in the image. In Fig. 4 we show polarized light images of the area between potential contacts in BaK122 crystals used in this study, with  $x=0.108$  (non-superconducting),  $x=0.202$  ( $T_c=10K$ ),  $x=0.235$  ( $T_c=26K$ ) and  $x=0.259$  ( $T_c=28K$ ). Images were taken on cooling at a temperature slightly above  $T_s$  and at base temperature. The highest contrast is observed when the sample is aligned with the [100] tetragonal direction at a 45° to the polarization direction of incident light (parallel and perpendicular to the orthorhombic  $a_o$  in different domains.) The contrast of domain images depends on the quality of the surface and the homogeneity of the samples. Domains are observed for samples with  $x \approx 0.26$ , and are no longer observed for

samples with higher doping level,  $x=0.34$ , which also do not show any features associated with structural transition in  $\rho(T)$ .

Selected samples were mounted for four-probe electrical resistivity measurements, with contacts made by soldering 50  $\mu\text{m}$  Ag wires using low-resistance Sn soldered contacts [34]. Initial resistivity measurements on each sample were carried out using a flexible wire arrangement with no strain applied to the sample (free standing state). The results are plotted in Fig. 5. Since this measurement is performed in the twinned state of the sample and contains contributions from both components of the in-plane resistivity in the orthorhombic phase, we call it  $\rho_t$ . Samples were then mounted on a brass horseshoe straining device, and strain was applied through the voltage contact wires by deformation of the horseshoe, see Ref. [7, 35] for the details of the procedure. Strain in this configuration is applied along the tetragonal [110] axis, which selects the orthorhombic  $a_o$  axis as a preferable direction upon cooling below  $T_S$ . Very soft current leads apply no strain. The strain was incrementally increased, and for each increment, temperature dependent resistivity measurements were made and the domain structure was imaged to determine the completeness of detwinning. Our previous studies using x-ray scattering have shown that when crystals are strained to the point at which no domains are visible in polarized microscopy, about 90 % of the whole bulk of the sample represents the domain whose orthorhombic  $a_o$  axis is oriented along the direction of the strain and therefore parallel to the current. Therefore in the detwinned state we are predominantly measuring the  $a_o$  axis resistivity,  $\rho_{a_o}$ , while in the unstrained state of the sample roughly equal contributions of both resistivity components are measured. Therefore, we may calculate the  $b_o$  axis resistivity,  $\rho_{b_o}(T)=2\rho_t(T) - \rho_{a_o}(T)$ .

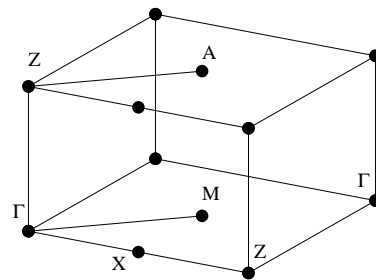


FIG. 6. The Brillouin zone of BaFe<sub>2</sub>As<sub>2</sub> corresponding to the two Fe unit cell.

### Contribution of the spin-fluctuation scattering

To justify the minimal model developed in Ref. [26], and used here to calculate the resistivity anisotropy shown in Fig. 3 of the main text, we use first-principles

band structure calculations. The first step is to unfold the first-principles Fermi surface from the two-Fe unit cell to an effective one-Fe unit cell, where the two magnetic ordering vectors are given by  $\mathbf{Q}_1 = (\pi, 0)$  and  $\mathbf{Q}_2 = (0, \pi)$ . In the Ba122 system, due to a sizeable hybridization with the As orbitals, there are two ways to unfold the overlapping and hybridized electron bands. One consists of constructing Wannier functions from a particular energy window (usually near the Fermi surface), symmetrizing them according to the primitive tetragonal group, and recalculating the band structure using the obtained Wannier functions [36]. This method provides a reasonable agreement of the folded bands with full DFT calculations, but this agreement may be achieved not through an appropriate As-induced hybridization, but through unphysically large one-electron hopping. The other method makes use of the actual symmetry element that reduces the larger unit cell to a smaller one: a glide plane. This method has been discussed in details in Ref. [37], and more briefly in Ref. [38]. It is this unfolding procedure that is appropriate for our purposes.

In the upper panel of Fig. 7 we show the DFT-calculated Fermi surface cross-sections by the plane  $k_z = 0$ . Because of the body-centered symmetry the point  $Z = (0, 0, \pi)$  is equivalent to  $(2\pi, 0, 0)$  (see Fig. 6 for notations). Therefore, the ellipticities of the electron pockets with respect to the point  $Z$  are opposite to those with respect to the point  $\Gamma$ . In the lower panel of Fig. 7 we show the Fermi surface cross-sections in the unfolded band from which the Fermi surface of the upper panel originates. In the unfolded zone, the ellipticity of the electron pockets with respect to  $Z$  is the same as with respect to  $\Gamma$ , but opposite as compared to the eccentricity with respect to  $M$  and  $A$  (see the notation in Fig. 6). After folding, the point  $M$  folds upon  $Z$ , and point  $A$  upon  $\Gamma$ , thus creating an impression that the ellipticity changes sign with  $k_z$ .

We note that there are two hole pockets at  $\Gamma Z$  but only one at  $MA$ , indicating that the dominating scattering processes are between the hole pockets at  $\Gamma Z$  and the electron pockets. This shows that the model of Ref. [26], considering a two-dimensional three band model with a circular hole pocket at the center  $\Gamma$  of the unfolded Brillouin zone and two elliptical electron pockets located at  $X = (\pi, 0)$  and  $Y = (0, \pi)$ , is an appropriate starting point. Within this model, the conductivity tensor is given by:

$$\sigma_{ij} = -e \sum_{\mathbf{k}, \lambda} v_{\mathbf{k}, \lambda}^i f_{\mathbf{k}, \lambda}^j$$

where  $v_{\mathbf{k}, \lambda}^i = \partial \varepsilon_{\mathbf{k}, \lambda} / \partial k_i$  is the component  $i$  of the Fermi velocity of band  $\lambda$  and  $f_{\mathbf{k}, \lambda}^j$  is the non-equilibrium electronic distribution function for a (unit) electric field applied along the  $j$  direction. The latter can be obtained by

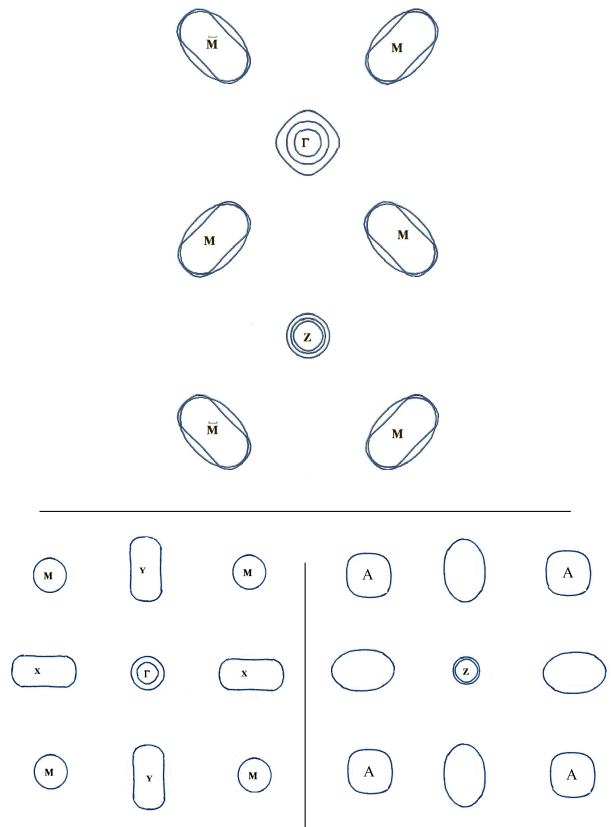


FIG. 7. Upper panel: First-principles calculated Fermi surface cross-sections for Ba122 in the folded Brillouin zone. Lower panels: the Fermi surface obtained from the unfolding procedure discussed in the text across  $k_z = 0$  (left panel) and  $k_z = \pi$  (right panel).

solving the Boltzmann equation in the presence of scattering by impurities and spin fluctuations, as explained in details in Ref. [26]. To obtain the results of Fig. 3, we followed the approach of Ref. [26], considering a putative magnetic quantum critical point and calculating numerically the temperature-dependent resistivity anisotropy. We used the same parameters as those of Ref. [26], varying the chemical potential to mimic the effects of hole doping and electron doping. For each value of the chemical potential, we obtained the complete temperature-dependence of the paramagnetic resistivity anisotropy and then extracted the maximum anisotropy, obtaining the results of Fig. 3.

#### Contribution of the Dirac cones: first-principles calculations

In order to address the kinematic effect of the magnetically-reconstructed Fermi surface anisotropy, we calculated the transport anisotropy using the actual DFT band structure and the constant relaxation time approx-

imation. It has been established that GGA calculations, even though they overestimate the long-range ordered magnetic moment by about a factor of two, provide a better agreement with the experimental Fermi surface than DMFT calculations, which yield the correct magnetic moment [22]. This is, incidentally, another manifestation that not only the local fluctuations, accounted for in DMFT, but also nematic fluctuations, consistent with a short range magnetic order of several lattice parameters, are responsible for the reduction of the ordered moment [16]. With this in mind, we used full potential LAPW bands, with full GGA magnetization, including spin-orbit interaction, to compute the Fermi surfaces and the Fermi velocities.

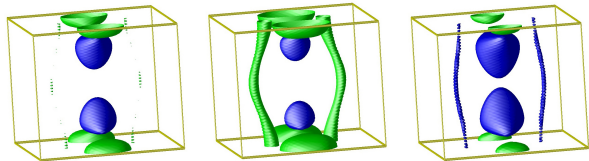


FIG. 8. The Fermi surface calculated deep inside the magnetically ordered phase for parent (left panel) electron- (middle panel) and hole - doped (right panel) compositions. Green - electron pockets, blue - hole pockets.

The Fermi surface calculated deep inside the magnetically ordered phase of the parent compound, shown in the left panel of Fig. 8, displays two sets of quasi-isotropic pockets: one for the holes (blue) and one for the electrons (green). It also displays barely visible threads, corresponding to the Dirac cones. They are green, indicating that in the calculations the Dirac points are located very slightly below, but practically at the Fermi level. Shifting the Fermi level up by 30 meV transforms the Dirac pockets into clearly visible electron tubes (middle panel in Fig. 8), while moving it down (right panel in Fig. 8) creates hole tubes instead. As pointed out in Ref. [39], the Fermi velocity in the Dirac cones is high, therefore whenever they are present, they dominate the transport. Near the Dirac point, the contribution from a Dirac cone to transport is  $Nv_F^2 \propto |E|$ , where  $E$  is the energy distance from the Dirac point.

Using an extrafine mesh of about 60000 inequivalent  $k$ -points ( $44 \times 44 \times 40$  divisions in the full Brillouin zone) we have calculated the transport function  $Nv_F^2(E)$  as a function of energy, separately for the hole bands and electron bands. One can see very clearly two regimes: one, where both regular and Dirac electrons contribute, and the other, where the latter contribution disappears. Except very near the Dirac point itself, Dirac electrons dominate transport. Moreover, contrary to the assumption in Ref. [39], the anisotropy comes mostly from the Dirac cones, and not from the “round” pockets. As Fig. 9 shows, the total anisotropy is vanishingly small when the

Fermi level is crossing the Dirac cones right at the Dirac point, which happens for  $E \approx E_F$  in the calculation. Away from this chemical potential, the anisotropy grows, retaining its positive value  $\rho_b/\rho_a > 1$ , for either hole or electron doping away from this point.

In the calculation, the Dirac point is very near the Fermi level for the undoped compound. To determine where it is in the real material, we can use the ARPES data of Ref. [28], or preferably, the quantum oscillation measurements of Ref. [22]. In the latter work, the authors observe that in order to bring the Dirac cone area into a complete agreement with the experiment, they need to shift the Fermi level in their LDA calculations up by 30 meV. In the former work, it was observed that the Dirac points are located 30 meV below the actual Fermi level. At the same time, they observed a factor of about three in the effective mass renormalization, implying that, in the unrenormalized band structure, the corresponding shift of the Fermi level would be 90 meV.

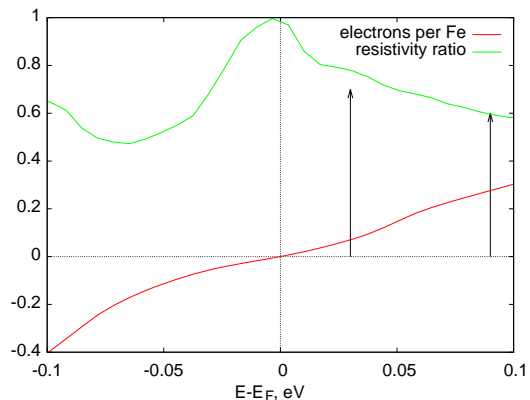


FIG. 9. The hole per Fe filling factor (lower curve) and the resistivity ratio,  $\rho_a/\rho_b$  (upper curve) obtained using band structure calculation, as described in the text. Note that the “as-calculated” Dirac points lie precisely on the Fermi level, and the resistivity anisotropy is essentially zero. In order to match the calculated Fermi surfaces with ARPES and quantum-oscillation experiments, respectively [22, 28], one needs to shift the calculated Fermi level of  $\text{BaFe}_2\text{As}_2$ , correspondingly, by 30 meV and 90 meV shifts. The resulting positions are indicated by arrows. After these shifts are applied, the minimal anisotropy ( $\rho_a/\rho_b \approx 1$ ) appear at the left of the arrows, that is to say, in the hole doping regime. Note that no symmetry demands that  $\rho_a/\rho_b$  be less than 1, small variation in the calculated band structure could render it slightly larger than 1, as observed in the experiment.

One could actually restrict the integration to particular parts of the Brillouin zone and separate the Dirac contribution from the rest. After that, one could shift the Dirac bands by the amount suggested by the experiment, and the other bands by their measured shift. This is however unnecessary, because the anisotropy is dominated by the Dirac band, and shifts of the other bands

do not really matter. Therefore, we calculated the total anisotropy as a function of doping, using straight DFT band structure, and simply marked (Fig. 9) the position of the Fermi level of the parent compound corresponding to the aforementioned 30 meV and 90 meV shifts. Note that the minimal anisotropy, which corresponds to 0.03-0.1 h/Fe depending on the shift, is nearly zero, but this is accidental; it could be a small positive or a small negative number (as in the experiment). DFT certainly does not describe these compounds at the level of accuracy sufficient to distinguish between these possibilities. Yet, it consistently describes the vanishing resistivity anisotropy in the magnetically ordered phase as holes are doped into the system.

### ACKNOWLEDGEMENTS

We thank A. V. Chubukov for useful comments, suggestions and critical reading of the manuscript. RMF and JS acknowledge useful discussions with E. Abrahams. Work at The Ames Laboratory was supported by the U.S. Department of Energy, Office of Basic Energy Sciences, Division of Materials Sciences and Engineering under contract No. DE-AC02-07CH11358. The work in China was supported by the NSF of China, the Ministry of Science and Technology of China (973 projects: 2011CBA00102, 2012CB821403). RMF acknowledges the support of the NSF Partnerships for International Research and Education (PIRE) program OISE-0968226.

- 
- [1] E. Fradkin, S. A. Kivelson, M. J. Lawler, J. P. Eisenstein, and A. P. Mackenzie. Nematic Fermi Fluids in Condensed Matter Physics. *Annu. Rev. Condens. Matter Phys.* **1**, 153 (2010).
- [2] K. B. Cooper, M. P. Lilly, J. P. Eisenstein, L. N. Pfeiffer, and K. W. West. Onset of anisotropic transport of two-dimensional electrons in high Landau levels: Possible isotropic-to-nematic liquid-crystal phase transition. *Phys. Rev. B* **65**, 241313(R) (2002).
- [3] R. A. Borzi, S. A. Grigera, J. Farrell, R. S. Perry, S. J. S. Lister, S. L. Lee, D. A. Tennant, Y. Maeno, and A. P. Mackenzie. Formation of a Nematic Fluid at High Fields in  $\text{Sr}_3\text{Ru}_2\text{O}_7$ . *Science* **315**, 214 (2006).
- [4] M. J. Lawler, K. Fujita, J. Lee, A. R. Schmidt, Y. Kohsaka, C. K. Kim, H. Eisaki, S. Uchida, J. C. Davis, J. P. Sethna, and Eun-Ah Kim. Intra-unit-cell electronic nematicity of the high- $T_c$  copper-oxide pseudogap states. *Nature* **466**, 374 (2010).
- [5] I. R. Fisher, L. Degiorgi, and Z. X. Shen. In-plane electronic anisotropy of underdoped '122' Fe-arsenide superconductors revealed by measurements of detwinned single crystals. *Rep. Prog. Phys.* **74**, 124506 (2011).
- [6] J.-H. Chu, J. G. Analytis, K. De Greve, P. L. McMahon, Z. Islam, Y. Yamamoto, and I. R. Fisher. In-Plane Resistivity Anisotropy in an Underdoped Iron Arsenide Superconductor. *Science* **329**, 824 (2010).
- [7] M. A. Tanatar, E. C. Blomberg, A. Kreyssig, M. G. Kim, N. Ni, A. Thaler, S. L. Bud'ko, P. C. Canfield, A. I. Goldman, I. I. Mazin, and R. Prozorov. Uniaxial-strain mechanical detwinning of  $\text{CaFe}_2\text{As}_2$  and  $\text{BaFe}_2\text{As}_2$  crystals: Optical and transport study. *Phys. Rev. B* **81**, 184508 (2010).
- [8] J. Paglione and R. L. Greene. High-temperature superconductivity in iron-based materials. *Nat. Phys.* **6**, 645 (2010).
- [9] D. C. Johnston. The puzzle of high temperature superconductivity in layered iron pnictides and chalcogenides. *Adv. Physics* **59** 803 (2010).
- [10] C. de la Cruz, Q. Huang, J. W. Lynn, J. Y. Li, W. Ratcliff, J. L. Zarestky, H. A. Mook, G. F. Chen, J. L. Lou, N. L. Wang, and P. C. Dai. Magnetic order close to superconductivity in the iron-based layered  $\text{LaO}_{1-x}\text{F}_x\text{FeAs}$  systems. *Nature* **453**, 899 (2008).
- [11] M. Yi, D. Lu, J.-H. Chu, J. G. Analytis, A. P. Sorini, A. F. Kemper, B. Moritz, S.-K. Mo, R. G. Moore, M. Hashimoto, W. S. Lee, Z. Hussain, T. P. Devereaux, I. R. Fisher, Z.-X. Shen. Symmetry-breaking orbital anisotropy observed for detwinned  $\text{Ba}(\text{Fe}_{1-x}\text{Co}_x)_2\text{As}_2$  above the spin density wave transition. *Proc. Nat. Acad. Sci.* 2011 **108**, 6878 (2011).
- [12] S. Kasahara, H. J. Shi, K. Hashimoto, S. Tonegawa, Y. Mizukami, T. Shibauchi, K. Sugimoto, T. Fukuda, T. Terashima, A. H. Nevidomskyy, and Y. Matsuda. Electronic nematicity above the structural and superconducting transition in  $\text{BaFe}_2(\text{As}_{1-x}\text{P}_x)_2$ . *Nature* **486**, 382 (2012)
- [13] J.-H. Chu, H.-H. Kuo, J. G. Analytis, and I. R. Fisher. Divergent Nematic Susceptibility in an Iron Arsenide Superconductor. *Science* **337**, 710 (2012).
- [14] C. Fang, H. Yao, W.-F. Tsai, J. Hu, and S. A. Kivelson. Theory of electron nematic order in  $\text{LaFeAsO}$ . *Phys. Rev. B* **77**, 224509 (2008).
- [15] C. Xu, M. Muller, and S. Sachdev. Ising and spin orders in the iron-based superconductors *Phys. Rev. B* **78**, 020501(R) (2008).
- [16] I. I. Mazin and M. D. Johannes. A key role for unusual spin dynamics in ferropnictides. *Nature Phys.* **5**, 141 (2009).
- [17] R. M. Fernandes, A. V. Chubukov, J. Knolle, I. Eremin, and J. Schmalian. Preemptive nematic order, pseudogap, and orbital order in the iron pnictides. *Phys. Rev. B* **85**, 024534 (2012).
- [18] M. A. Tanatar, A. Kreyssig, S. Nandi, N. Ni, S. L. Bud'ko, P. C. Canfield, A. I. Goldman, and R. Prozorov. Direct imaging of the structural domains in the iron pnictides  $\text{AFe}_2\text{As}_2$  (A=Ca,Sr,Ba). *Phys. Rev. B* **79**, 180508 (2009)
- [19] E. C. Blomberg, A. Kreyssig, M. A. Tanatar, R. M. Fernandes, M. G. Kim, A. Thaler, J. Schmalian, S. L. Bud'ko, P. C. Canfield, A. I. Goldman, and R. Prozorov. Effect of tensile stress on the in-plane resistivity anisotropy in  $\text{BaFe}_2\text{As}_2$ . *Phys. Rev. B* **85**, 144509 (2012).
- [20] R. M. Fernandes, L. H. VanBebber, S. Bhattacharya, P. Chandra, V. Keppens, D. Mandrus, M. A. McGuire, B. C. Sales, A. S. Sefat, and J. Schmalian. Effects of Nematic Fluctuations on the Elastic Properties of Iron Arsenide Superconductors. *Phys. Rev. Lett.* **105**, 157003 (2010).



- [21] J.J. Ying, X.F. Wang, T. Wu, Z.J. Xiang, R.H. Liu, Y.J. Yah, A.F. Wang, M. Zhang, G.J. Ye, P. Cheng, J.P. Hu, X.H. Chen. Measurements of the Anisotropic In-Plane Resistivity of Underdoped FeAs-Based Pnictide Superconductors. *Phys. Rev. Lett.* **107**, 067001 (2011).
- [22] T. Terashima, N. Kurita, M. Tomita, K. Kihou, C.-H. Lee, Y. Tomioka, T. Ito, A. Iyo, H. Eisaki, T. Liang, M. Nakajima, S. Ishida, Shin-ichi Uchida, H. Harima, and S. Uji. Complete Fermi Surface in BaFe<sub>2</sub>As<sub>2</sub> Observed via Shubnikov-de Haas Oscillation Measurements on Detwinned Single Crystals. *Phys. Rev. Lett.* **107**, 176402 (2011).
- [23] C.-C. Chen, J. Maciejko, A. P. Sorini, B. Moritz, R. R. P. Singh, and T. P. Devereaux. Orbital order and spontaneous orthorhombicity in iron pnictides. *Phys. Rev. B* **82**, 100504 (2010).
- [24] W. Lv and P. Phillips. Orbital and magnetically induced anisotropy in iron-based superconductors. *Phys. Rev. B* **84**, 174512 (2011).
- [25] E. Bascones, M.J. Calderon, and B. Valenzuela. Low Magnetization and Anisotropy in the Antiferromagnetic State of Undoped Iron Pnictides. *Phys. Rev. Lett.* **104**, 227201 (2010).
- [26] R. M. Fernandes, E. Abrahams, and J. Schmalian. Anisotropic In-Plane Resistivity in the Nematic Phase of the Iron Pnictides. *Phys. Rev. Lett.* **107**, 217002 (2011).
- [27] S. Liang, G. Alvarez, C. Sen, A. Moreo, and E. Dagotto. Anisotropy of Electrical Transport in Pnictide Superconductors Studied Using Monte Carlo Simulations of the Spin-Fermion Model. *Phys. Rev. Lett.* **109**, 047001 (2012).
- [28] T. Shimojima, K. Ishizaka, Y. Ishida, N. Katayama, K. Ohgushi, T. Kiss, M. Okawa, T. Togashi, X.-Y. Wang, C.-T. Chen, S. Watanabe, R. Kadota, T. Oguchi, A. Chainani, and S. Shin. Orbital-Dependent Modifications of Electronic Structure across the Magnetostructural Transition in BaFe<sub>2</sub>As<sub>2</sub>. *Phys. Rev. Lett.* **104**, 057002 (2010); Yeongkwan Kim, Hyungju Oh, Chul Kim, Dongjoon Song, Wonsig Jung, Beomyoung Kim, Hyoung Joon Choi, Changyoung Kim, Bumsung Lee, Seunghyun Khim, Hyungjoon Kim, Keehoon Kim, Jongbeom Hong, and Yongseung Kwon. Electronic structure of detwinned BaFe<sub>2</sub>As<sub>2</sub> from photoemission and first principles. *Phys. Rev. B* **83**, 064509 (2011).
- [29] Juan Jiang, C. He, Y. Zhang, M. Xu, Q. Q. Ge, Z. R. Ye, F. Chen, B. P. Xie, D. L. Feng. The distinct in-plane resistivity anisotropy in the nematic states of detwinned NaFeAs and FeTe single crystals: evidences for Hund's rule metal. arXiv:1210.0397
- [30] N. D. Mathur, F. M. Grosche, S. R. Julian, I. R. Walker, D. M. Freye, R. K. W. Haselwimmer, and G. G. Lonzarich. Magnetically mediated superconductivity in heavy fermion compounds. *Nature* **394**, 39 (1998).
- [31] L. Taillefer. Scattering and Pairing in Cuprate Superconductors. *Annu. Rev. Condens. Matter Phys.* **1**, 51 (2010).
- [32] H. Q. Luo, Z. S. Wang, H. Yang, P. Cheng, X. Zhu, and H.-H. Wen. Growth and characterization of A<sub>1-x</sub>K<sub>x</sub>Fe<sub>2</sub>As<sub>2</sub> (A = Ba, Sr) single crystals with x = 0-0.4. *Supercond. Sci. Technol.* **21**, 125014 (2008).
- [33] M. A. Tanatar, E. C. Blomberg, Hyunsoo Kim, Kyuil Cho, W. E. Straszheim, Bing Shen, Hai-Hu Wen, R. Prozorov. Anisotropic resistivity in underdoped single crystals, 0 ≤ x < 0.35. arXiv:1106.0533
- [34] M. A. Tanatar, N. Ni, S. L. Bud'ko, P. C. Canfield, and R. Prozorov. Field-dependent transport critical current in single crystals of Ba(Fe<sub>1-x</sub>TM<sub>x</sub>)<sub>2</sub>As<sub>2</sub> (TM = Co, Ni) superconductor. *Supercond. Sci. Technol.* **23**, 054002 (2010).
- [35] E. C. Blomberg, M. A. Tanatar, A. Kreyssig, N. Ni, A. Thaler, Rongwei Hu, S. L. Bud'ko, P. C. Canfield, A. I. Goldman, and R. Prozorov. In-plane anisotropy of electrical resistivity in strain-detwinned SrFe<sub>2</sub>As<sub>2</sub>. *Phys. Rev. B* **83**, 134505 (2011).
- [36] S. Graser, A. F. Kemper, T. A. Maier, H.-P. Cheng, P. J. Hirschfeld, and D. J. Scalapino. Spin fluctuations and superconductivity in a three-dimensional tight-binding model for BaFe<sub>2</sub>As<sub>2</sub>. *Phys. Rev. B* **81**, 214503 (2010).
- [37] O.K. Andersen, L. Boeri. On the multi-orbital band structure and itinerant magnetism of iron-based superconductors. *Annalen der Physik*, **1**, 8-50 (2011).
- [38] P.J. Hirschfeld, M.M. Korshunov, I.I. Mazin. Gap symmetry and structure of Fe-based superconductors. *Reports on Progress in Physics* **74**, 124508 (2011).
- [39] H.-H. Kuo, J.-H. Chu, S. C. Riggs, L. Yu, P. L. McMahon, K. De Greve, Y. Yamamoto, J. G. Analytis and I. R. Fisher. Possible origin of the nonmonotonic doping dependence of the in-plane resistivity anisotropy of Ba(Fe<sub>1-x</sub>T<sub>x</sub>)<sub>2</sub>As<sub>2</sub> (T=Co, Ni and Cu). *Phys. Rev. B* **84**, 054540 (2011).